ACS APPLIED MATERIALS & INTERFACES
Research Article
www.acsami.org

Dual-Phase Glass Ceramic: Structure, Dual-Modal Luminescence, and Temperature Sensing Behaviors

Daqin Chen,*[†] Zhongyi Wan,[†] Yang Zhou,[†] Xiangzhi Zhou,[‡] Yunlong Yu,[§] Jiasong Zhong,[†] Mingye Ding,[†] and Zhenguo Ji[†]

[†]College of Materials & Environmental Engineering, Hangzhou Dianzi University, Hangzhou 310018, P. R. China
[‡]Hangzhou Guangrong Science and Technology Co. Ltd., Hangzhou 310018, P. R. China
[§]College of Electronics and Information Science, Fujian Jiangxia University, Fuzhou, Fujian 350108, P. R. China

ABSTRACT: $Yb^{3+}/Er^{3+}/Cr^{3+}$ triply doped transparent bulk glass ceramic containing orthorhombic YF_3 and cubic Ga_2O_3 nanocrystals was fabricated by a melt-quenching route to explore its possible application in optical thermometry with high spatial and temperature resolution. It was experimentally observed that Yb^{3+}/Er^{3+} ions incorporated into the precipitated YF_3 nanophase, while Cr^{3+} ions partitioned into the crystallized Ga_2O_3 nanophase after glass crystallization. Importantly, such spatial isolation strategy efficiently suppressed adverse energy transfer among different active ions. As a consequence, intense green anti-Stokes luminescence originated from Er^{3+}: $^2H_{11/2},^4S_{3/2} \rightarrow {}^4I_{15/2}$ transitions, and deep-red Stokes luminescence transitions assigned to Cr^{3+}: $^2E \rightarrow {}^4A_2$ radiation were simultaneously realized. Impressively, the intermediate crystal-field environment for Cr^{3+} in Ga_2O_3 made it possible for lifetime-based temperature sensing owing to the competition of radiation transitions from the thermally coupled Cr^{3+} ^2E and $^4T_2$ excited states. In the meantime, the low-phonon-energy environment for Er^{3+} in YF_3 was beneficial for upconversion fluorescence intensity ratio-based temperature sensing via thermal population between the $^2H_{11/2}$ state and $^4S_{3/2}$ state. The Boltzmann distribution theory and the two-level kinetic model were adopted to interpret these temperature-dependent luminescence of Er^{3+} and Cr^{3+}, respectively, which gave the highest temperature sensitivities of 0.25% K^{-1} at 514 K for Er^{3+} and 0.59% K^{-1} at 386 K for Cr^{3+}.

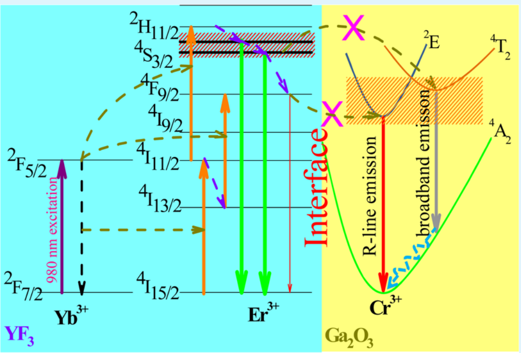

KEYWORDS: *glass ceramic, upconversion, nanocrystal, lanthanide, temperature sensing*

INTRODUCTION

Temperature is a fundamental physical quantity which is essential in both industrial and scientific fields. Generally, traditional contact temperature sensors require direct heat transfer and subsequent thermal equilibrium between the measured object and the sensor. This usually needs a long time during the measurement and may change the actual temperature of sample, especially when the size of the sample is small or comparable to that of the sensor head. Therefore, it is quite meaningful to measure temperature with high spatial and temperature resolution. Recently, some efforts have been focused on the study of the temperature-dependent rare earth (RE) ions doped anti-Stokes (or upconversion, UC) emission or transition-metal (TM) ions doped Stokes emission material owing to their significant potential application in noncontact temperature sensors.[1−6] Generally, optical parameters, such as the fluorescence intensity, the peak wavelength, the emission bandwidth, the fluorescence intensity ratio (FIR), as well as the fluorescence lifetime, can be adopted to detect temperature.[7−12] Unfortunately, the fluorescence intensity, the peak wavelength, and the emission bandwidth are strongly affected by the external factor, such as light source, atmosphere, and pressure. In contrast, FIR-based temperature sensors exhibit a high measurement accuracy and reliability because FIR is independent of spectral losses and fluctuations in the excitation density. Besides, fluorescence-lifetime-based temperature sensors have advantages of intrinsic immunity to electromagnetic interference and calibration-free measurement, and find promising applications in harsh environments, such as building fire detection, corrosive surrounding, and microwave induction heating, where traditional temperature sensors are not feasible.[13,14]

Notably, trivalent TM ions (such as Cr^{3+}) doped luminescent materials are particularly favored for fluorescence-lifetime-based temperature sensing owing to the great variety in the temperature-dependent lifetime.[15−18] Generally, Cr^{3+} with $3d^3$ electron configuration exhibits a broad emission band (650−1600 nm) ascribed to the $^4T_2 \rightarrow {}^4A_2$ transition, or a narrow emission band (∼700 nm) due to the $^2E \rightarrow {}^4A_2$ radiation, which strongly depends on the crystal-field environment of the host lattices. In the intermediate or high strength crystal field, such as

Received: July 6, 2015
Accepted: August 19, 2015
Published: August 19, 2015

Table 1. Chemical Compositions for the Studied Samples

	chemical composition in mol %										
sample	SiO_2	Al_2O_3	YF_3	Ga_2O_3	NaF	LiF	YbF_3	ErF_3	Cr_2O_3	crystallization condition	crystallization phase
GC-A	40	20	13.9	9.9	7	8	1	0.1	0.1	720 °C/2 h	Ga_2O_3 + YF_3
GC-B	40	20		9.9	15	15			0.1	650 °C/2 h	Ga_2O_3
GC-C	44	28	15.9		11		1	0.1		670 °C/2 h	YF_3

in ruby and alexandrite,[19,20] ^2E is the lowest excited state, and the transition of $^2E \rightarrow {}^4A_2$ is doubly forbidden by parity and spin, which shows a long decay lifetime, while in a low strength crystal field, $^4T_2$ is the lowest excited state and the transition of $^4T_2 \rightarrow {}^4A_2$ is spin-allowed, which results in a short decay lifetime. As a consequence, significant variety in temperature-dependent lifetime can be expected, and a useful level control is made possible by modifying the crystal-field strength via the variation of the host material. On the other hand, trivalent RE ion (such as Yb^{3+}/Er^{3+}) doped UC materials are advantageous for FIR-based thermometric applications due to the obvious temperature-dependent emissions that originated from the two thermally coupled Er^{3+} $H_{11/2}$ and $^4S_{3/2}$ emitting states.[8,9,21,22] In order to advance their direct applications in highly sensitive temperature sensing, it is quite valuable to explore optical materials with multifunctionality, for example, exhibiting both temperature-dependent UC FIR and temperature-dependent decay lifetime. However, as far as we know, there is no report concerning the achievement of both temperature-dependent UC FIR of Er^{3+} and temperature-dependent decay lifetime of Cr^{3+} in a sole host so far. In fact, adverse energy transfers (ETs) between RE and TM usually occur ascribing to their energy level matching when they are codoped into the same host, which subsequently leads to the luminescent quenching for both activators.[23−25] Therefore, seeking special hosts to realize dual-modal temperature-dependent luminescence of both RE and TM remains a formidable challenge, but is highly desirable.

Currently, most of the reported optical materials for FIR or lifetime based thermometric applications are powders and single crystals. However, the scattering of the powder phosphors is serious; the fabrication of monocrystal is extremely time-consuming and complex, and some crystals may not be readily grown as bulk materials owing to the occurrence of phase transformation.[26] As an alternative, transparent glass ceramic (GC) composites have gained wide attention over recent years.[27−35] GCs can be fabricated via the simple preparation process of the common glass, which is beneficial to large-scale production, high transparency, a wide range of accessible chemical compositions and fabrication of complex shapes. Importantly, the partition of the active centers into the precipitated crystalline phase by controlling glass crystallization is one of the key factors for the efficient luminescence of GC.

Herein, RE (Yb^{3+}/Er^{3+}) and TM (Cr^{3+}) codoped aluminosilicate glass with special designed chemical composition of $SiO_2-Al_2O_3-YF_3-Ga_2O_3-NaF-LiF$ was successfully fabricated by a melt-quenching route. To suppress adverse energy transfers between Er^{3+} and Cr^{3+}, glass crystallization strategy was successfully applied to convert the precursor glass into nanostructured GC containing YF_3 and Ga_2O_3 dual-crystalline phases. Importantly, RE ions were evidenced to incorporate into the precipitated orthorhombic YF_3 nanophase, while Cr^{3+} ones entered into the cubic Ga_2O_3 nanoparticles. Such spatial separation of different active ions can effectively suppress adverse energy transfers between Er^{3+} and Cr^{3+}, leading to both intense anti-Stokes luminescence of Er^{3+} and Stokes luminescence of Cr^{3+} in GC. Furthermore, the influence of temperature on the emission spectra and decay behaviors of the thermally coupled $H_{11/2}$ and $^4S_{3/2}$ emitting states of Er^{3+} as well as the ^2E and $^4T_2$ ones of Cr^{3+} in this dual-phase GC was systematically studied to explore its possible application in the optical temperature sensors.

EXPERIMENTAL DETAILS

The precursor glass (PG) with the chemical composition (mol %) of $40SiO_2-20Al_2O_3-15YF_3-10Ga_2O_3-7NaF-8LiF-1YbF_3-0.1ErF_3-0.1Cr_2O_3$ was prepared by a melt-quenching route. The chemicals were mixed thoroughly and melted in a covered alumina crucible at 1450 °C for 1 h in the air atmosphere. Then, the melt was poured into 300 °C preheated copped mold and cooled down naturally to room temperature to relinquish the inner stress in the precursor glass. Afterward, the PG was heat-treated at 720 °C for 2 h to form dual-phase transparent glass ceramics (donated as GC-A) via glass crystallization. As a comparison, single-phase crystal-embedded transparent GCs (donated as GC-B and GC-C for Ga_2O_3 embedded GC and YF_3 embedded GC, respectively) were also fabricated by a similar process. The compositions of glasses, the crystallization conditions, and the precipitated phases are given in Table 1.

To determine actual glass composition, X-ray photoelectron spectroscopy (XPS, VG Scientific ESCA Lab Mark II) measurement was carried out. C_{1s} peak (284.8 eV) of the surface adventitious carbon was adopted as the reference. To identify the crystallization phase and determine the mean size of the precipitated crystals in glass matrix, X-ray diffraction (XRD) analysis was carried out with a powder diffractometer (DMAX2500 RIGAKU) using Cu Kα radiation (λ = 0.154 nm). The microstructure of GC sample was studied using a transmission electron microscopy (TEM, JEM-2010) equipped with the selected area electron diffraction (SAED). TEM specimen was prepared by directly drying a drop of a dilute ethanol dispersion solution of GC pieces on the surface of a carbon coated copper grid. The photoluminescence (PL) spectra, PL excitation (PLE) spectra, UC emission spectra, as well as decay curves of PG and GC samples were recorded on an Edinburgh Instruments (EI) FS5 spectrofluorometer equipped with both continuous (150 W) and pulsed xenon lamps. The 980 nm laser diode (MDL-III-980 nm-1W, Edinburgh Instruments) with tunable output power (0−1 W) and a stabilized controller PM1 was used as the UC excitation source. The power density for the measurement of temperature-dependent UC emission spectra was 20 W/cm^2. The temperature-dependent UC spectra and luminescent decay curves were detected on FS5 spectrofluorometer equipped with a homemade temperature controlling stage.

RESULTS AND DISCUSSION

To determine the actual glass composition, XPS measurement was carried out on the glass sample with nominal composition of $40SiO_2-20Al_2O_3-15YF_3-10Ga_2O_3-7NaF-8LiF-1YbF_3-$

$0.1ErF_3$–$0.1Cr_2O_3$. As shown in Table 2, the actual contents of Y, Na, Li, Yb, and F elements are slightly lower than the nominal ones, attributing to high temperature evaporation of raw fluoride materials during glass melting. The Er and Cr contents are under the detecting limit. Notably, a small amount of fluoride volatilization has no obvious influence on YF_3 and Ga_2O_3 crystallization and the related optical performance for the investigated glass ceramics. XRD patterns of the PG and GC samples are provided in Figure 1. Apparently, for PG, only diffuse humps are observed, proving its amorphous feature. After glass crystallization treatment at 720 °C for 2 h, the GC-A sample shows shape diffraction peaks, which can be clearly assigned to the orthorhombic β-YF_3 crystal (JPCDS no. 74-0911) and the cubic γ-Ga_2O_3 one (JCPDS no. 20-0426) one. According to the Scherrer formula, the average sizes of γ-Ga_2O_3 and β-YF_3 particles in the dual-phase GC-A sample were determined to be 8 and 35 nm, respectively. As a comparison, XRD patterns of GC-B and GC-C samples (Figure 1) reveal the precipitation of cubic γ-Ga_2O_3 and orthorhombic β-YF_3 crystalline phases in the glass matrix, respectively. TEM micrograph of the GC720 sample, as shown in Figure 2a, presents two types of particles distributing homogeneously among aluminosilicate glass matrix, i.e., the larger nanocrystals (NCs) with size 25−45 nm and the smaller ones with size 5−10 nm. High resolution TEM (HRTEM) images and the corresponding FFT patterns of these two types of particles confirm their crystalline nature with high crystallinity. Evidently, the (400) crystalline plane of γ-Ga_2O_3 and the (111) one of β-YF_3 with the corresponding interplanar spacing of 2.1 and 3.2 Å are clearly marked in Figure 2b,c, respectively.

Table 2. Nominal and Actual Glass Composition (mol %)

element	nominal	actual
Si	11.14	11.31
Al	11.14	11.31
Y	3.87	3.76
Ga	5.51	5.60
Na	1.95	1.82
Li	2.23	2.03
Yb	0.28	0.26
O	47.26	47.97
F	16.62	15.94

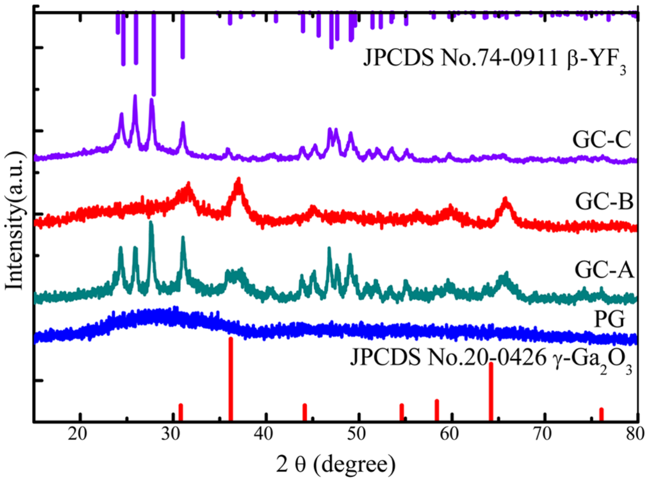

Figure 1. XRD patterns of PG, GC-A, GC-B, and GC-C samples. Bars represent standard cubic Ga_2O_3 (JCPDS no. 20-0426) and orthorhombic YF_3 diffraction data (JCPDS no. 74-0911).

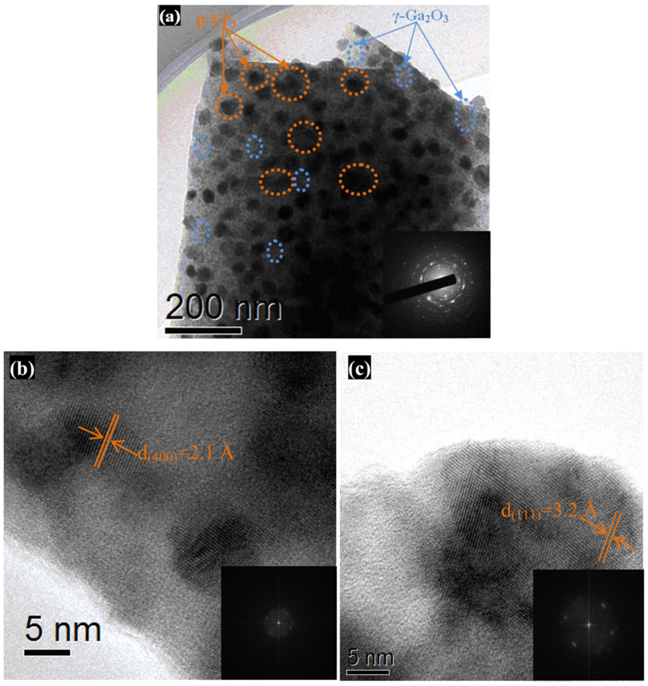

Figure 2. (a) TEM image of GC-A sample. Inset is the corresponding SAED pattern. HRTEM micrographs of (b) γ-Ga_2O_3 and (c) β-YF_3 nanoparticles. Insets are the corresponding fast Fourier transform (FFT) patterns.

To reveal the locations of Ln^{3+} and Cr^{3+} dopants in the dual-phase glass ceramic, optical spectroscopy of the PG and GC-A samples was systematically investigated, as shown in Figure 3. Under 980 nm near-infrared (NIR) laser excitation, both UC emission spectra of the $Yb^{3+}/Er^{3+}/Cr^{3+}$ triply doped PG and GC-A samples (Figure 3a) exhibit green (~539 nm) and red (~657 nm) UC emissions ascribed to ${}^2H_{11/2},{}^4S_{3/2} \rightarrow {}^4I_{15/2}$ and ${}^4F_{9/2} \rightarrow {}^4I_{15/2}$ transitions of Er^{3+} ions, respectively. Evidently, the UC luminescence of GC-A is much stronger than that of PG, i.e., about 10 times as high as that of the PG one, and the emission bands of GC-A become structured (Stark-splitting) and narrowed. This is believed to be attributed to the modification of Yb^{3+}/Er^{3+} surrounded from an amorphous glass environment to a crystalline one after glass crystallization. As revealed in the inset of Figure 3a, the Stark-splitting structures of Er^{3+} in the dual-phase glass ceramic (GC-A) are similar to the case of the Yb^{3+}/Er^{3+} doped YF_3 single-phase embedded glass ceramic (GC-C). Therefore, all these results suggest the partition of Yb^{3+} and Er^{3+} dopants in YF_3 crystalline lattice (by substituting Y^{3+} ions) instead of Ga_2O_3 in the present dual-phase GC, owing to the similar radii between Yb^{3+}/Er^{3+} (r = 0.87/0.89 Å, CN = 6) and Y^{3+} (r = 0.90 Å, CN = 6). This can be further confirmed by the much slower UC decay of Er^{3+} in GC-A than in PG, as shown in Figure 3b. Generally, for UC materials, a long lifetime indicates a highly efficient UC luminescence, i.e., a low nonradiative deactivation probability of Ln^{3+} activators.[36] As exhibited in Figure 3b, taking Er^{3+}: ${}^2H_{11/2},{}^4S_{3/2}$ emitting states as an example, the decay lifetime (0.750 ms) of GC-A is obviously longer than that (0.089 ms) of PG, owing to the low-phonon-energy YF_3 crystalline environment where Ln^{3+} dopants reside.

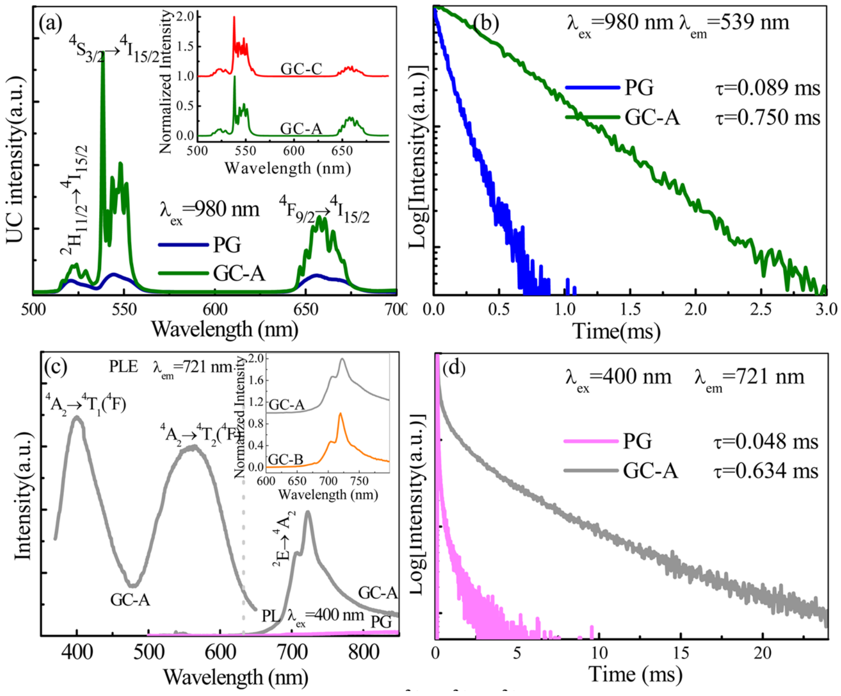

Figure 3. (a) UC emission spectra of the $Yb^{3+}/Er^{3+}/Cr^{3+}$ triply doped PG and GC-A samples under 980 nm laser excitation. Inset of part a is the normalized UC spectra of GC-A and GC-C samples. (b) Decay curves of the Er^{3+}: $^2H_{11/2}$,$^4S_{3/2}$ states in the PG and GC-A samples. (c) PLE (λ_{em} = 721 nm) and PL (λ_{ex} = 400 nm) spectra of the $Yb^{3+}/Er^{3+}/Cr^{3+}$ triply doped PG and GC-A samples. Inset of part c is the normalized PL spectra of GC-A and GC-B samples. (d) Decay curves of the Cr^{3+}:^2E state in the PG and GC-A samples.

Room temperature PL/PLE spectra of $Yb^{3+}/Er^{3+}/Cr^{3+}$ triply doped PG and GC-A samples under 400 nm blue light excitation are provided in Figure 3c. GC sample shows a sharp emission line (~721 nm) assigned to the Cr^{3+} $^2E \to {}^4A_2$ spin-forbidden transition. The associated broad background emission in the wavelength range 650−850 nm originates from the phonon sidebands of the $^4T_2 \to {}^4A_2$ transition. The PL excitation (PLE) spectrum of GC-A (Figure 3c) monitored at 721 nm emission covers a very broad spectral region from 350 to 650 nm and consists of two broad excitation bands that peaked at 400 and 562 nm, attributed to the spin-allowed $^4A_2 \to {}^4T_1(^4F)$ and $^4A_2 \to {}^4T_2(^4F)$ absorption transitions of Cr^{3+}, respectively. Obviously, the emission intensity of GC-A is found to be far stronger than that of the corresponding PG, and the emission spectrum of GC-A resembles that of Cr^{3+} doped Ga_2O_3 single-phase embedded glass ceramic (GC-B, inset of Figure 3c), indicating the incorporation of Cr^{3+} into Ga_2O_3 crystalline lattice after glass crystallization. In fact, the doped Cr^{3+} ions prefer to occupy octahedral site of Ga^{3+} in Ga_2O_3 host because of the approximate ionic radii between Ga^{3+} (r = 0.620 Å, CN = 6) and Cr^{3+} (r = 0.615 Å, CN = 6) as well as the strong ligand-field stabilization energy of Cr^{3+} in 6-fold coordination.[37,38] Figure 3d shows the PL decay curves of Cr^{3+} in the PG and GC-A samples. The lifetime on the order of a millisecond is one of the features of the spin-forbidden $^2E \to {}^4A_2$ transition of Cr^{3+}.[23] Evidently, the longer lifetime of Cr^{3+} in GC-A (0.634 ms) than in PG (0.048 ms) further confirms the occupation of Cr^{3+} in crystalline environment.

In general, Cr^{3+} 3d electrons are strongly coupled to lattice vibration and affected by crystal-field strength and site symmetry of the host. Usually, the level scheme for Cr^{3+} in the host can be described using the Tanabe−Sugano diagram, as shown in Figure 4. The local crystal-field strength Dq and the Racah parameter B can be estimated by spectroscopic data using the following equations[39,40]

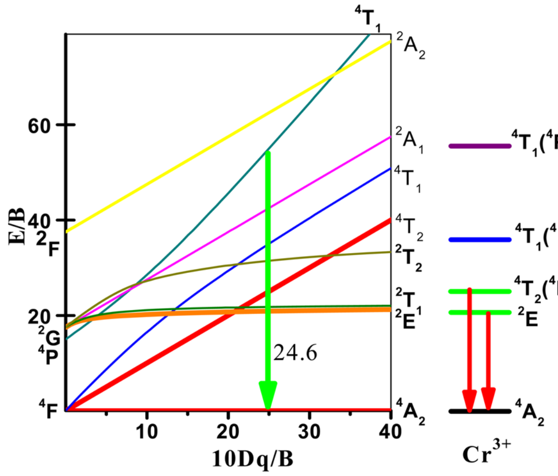

Figure 4. Tanabe−Sugano diagram of Cr^{3+} in the dual-phase GC sample.

$$\mathrm{Dq} = \frac{E(^4A_2 \to {}^4T_2)}{10} \tag{1}$$

$$\frac{\mathrm{Dq}}{B} = \frac{15(m-8)}{(m^2-10m)} \tag{2}$$

where the m value is determined with the help of the average peak energies of the $^4A_2 \to {}^4T_1$ and $^4A_2 \to {}^4T_2$ transitions of Cr^{3+}

$$m = \frac{E(^4A_2 \to {}^4T_1) - E(^4A_2 \to {}^4T_2)}{\mathrm{Dq}} \tag{3}$$

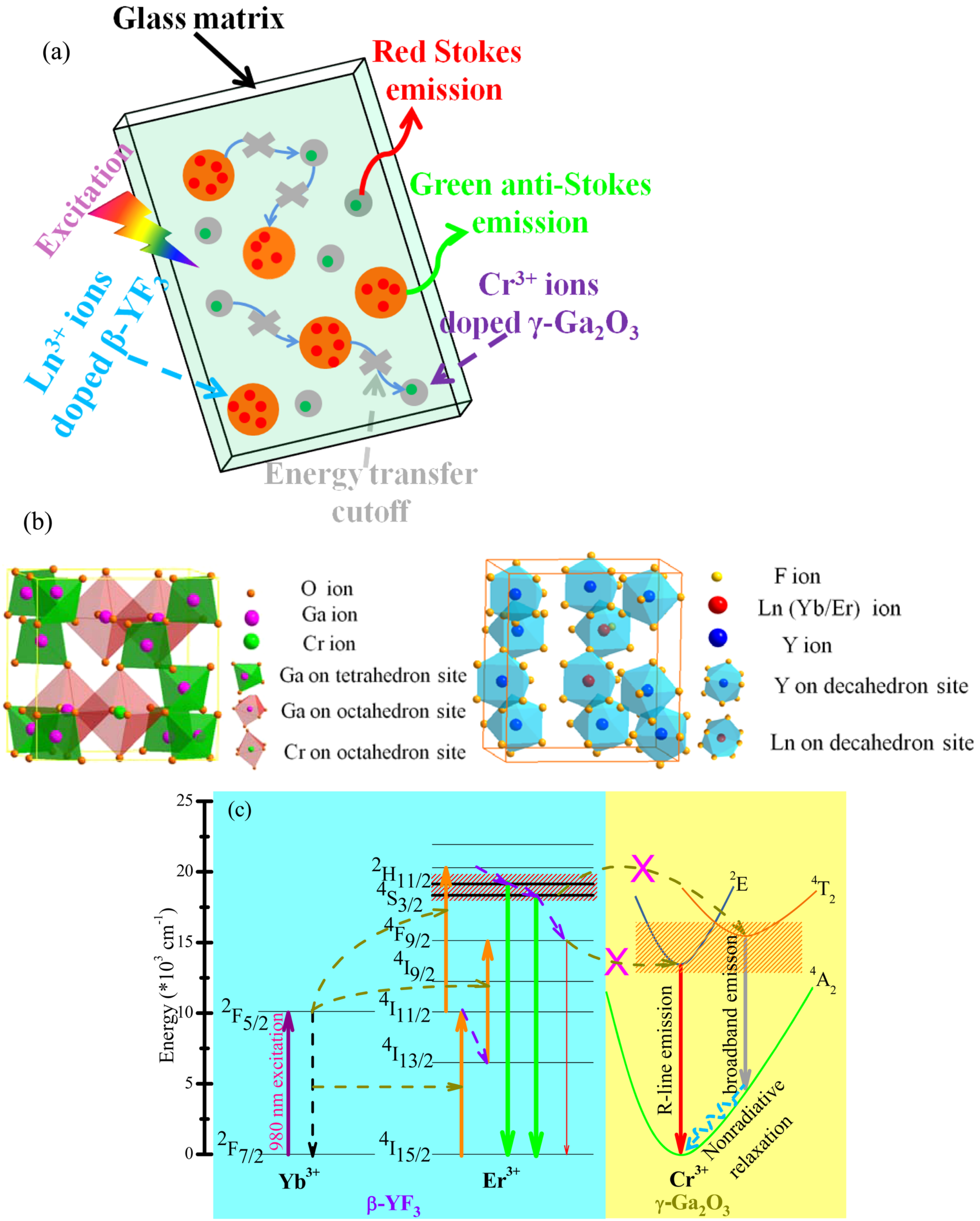

Figure 5. (a) Sketch showing the distribution and dual-modal luminescent behaviors of Yb^{3+}/Er^{3+} and Cr^{3+} ions in the dual-phase GC. (b) Left: Unit-cell structure of γ-Ga_2O_3. Pink spheres represent Ga^{3+} ions on tetrahedral and octahedral sites, and green spheres stand for Cr^{3+} ions substituting for Ga^{3+} ions which are on octahedral sites. Right: Unit-cell structure of β-YF_3. Blue spheres represent Y^{3+} ion on decahedron sites, and red spheres represent Yb^{3+}/Er^{3+} ions replacing Y^{3+} ions which are on decahedron sites. (c) Schematic energy level diagrams of Yb^{3+}, Er^{3+} and configuration coordination of Cr^{3+} showing the suppression of energy transfers between Er^{3+} and Cr^{3+} ions when Yb^{3+}/Er^{3+} partitioned into YF_3 while Cr^{3+} ions entered into Ga_2O_3.

According to the above expression, the Dq, *B*, and Dq/*B* values are evaluated to be 1779 cm^{-1}, 723 cm^{-1}, and 2.46, respectively, for the present dual-phase glass ceramic. The intermediate value of the parameter Dq/*B* for Cr^{3+} in GC-A suggests that the energy of the Cr^{3+}: $^4T_2(^4F)$ state is higher than that of Cr^{3+}: ^2E, which agrees with the existence of the dominant sharp emission band assigned to spin- and parity-forbidden Cr^{3+} $^2E \rightarrow {}^4A_2$ transition (Figure 3c).

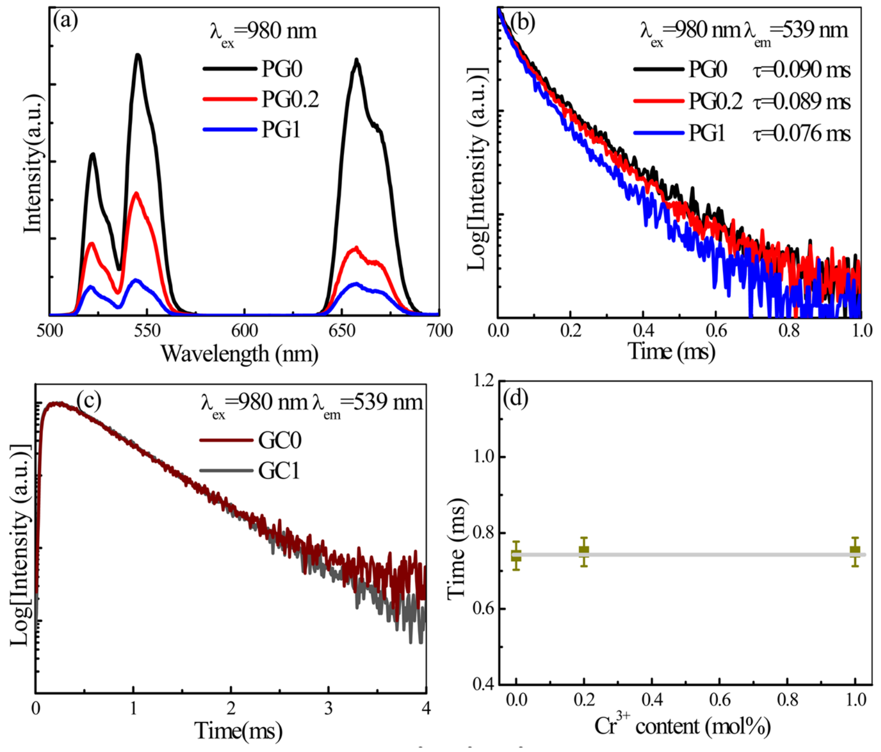

Figure 6. (a) UC emission spectra of the $Yb^{3+}/Er^{3+}/Cr^{3+}$ triply doped PG samples with various Cr^{3+} contents under 980 nm NIR laser excitation. The decay curves of the Er^{3+}: $^2H_{11/2}$,$^4S_{3/2}$ emitting states for the (b) PG and (c) GC samples. (d) The fluorescence decay lifetime versus Cr^{3+} content in the dual-phase GCs.

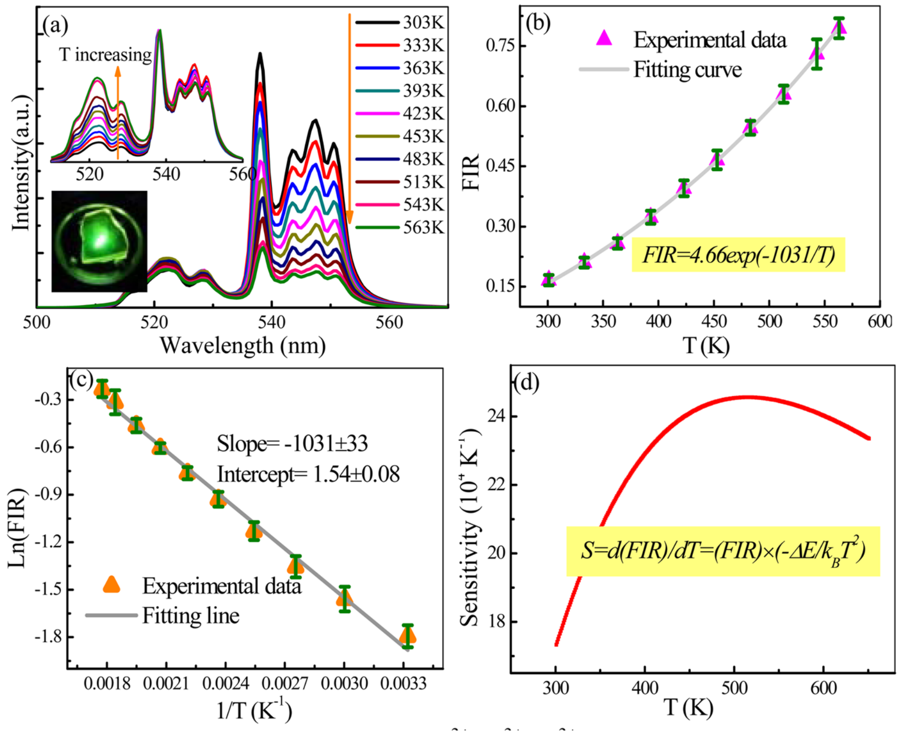

Figure 7. (a) UC emission spectra of the $Yb^{3+}/Er^{3+}/Cr^{3+}$ triply doped GC-A sample in the wavelength range 500−570 nm at different temperatures (303−563 K). Inset shows normalized spectra (top) and UC luminescent photograph (bottom). (b) Temperature dependence of FIR. (c) Monolog plot of FIR versus inverse absolute temperature. (d) Temperature dependence of sensor sensitivity.

On the basis of the above analysis, after glass crystallization, Cr^{3+} dopants partitioned into the precipitated Ga_2O_3 phase, which provides an intermediate crystal-field for Cr^{3+} and makes it possible for lifetime-based temperature sensing owing to the competition of radiation transitions from the thermal coupling Cr^{3+} ^2E and $^4T_2$ excited states. On the other hand, Yb^{3+}/Er^{3+} ions incorporated into the crystallized YF_3 phase which provides a low-phonon-energy environment for Er^{3+} and makes it suitable

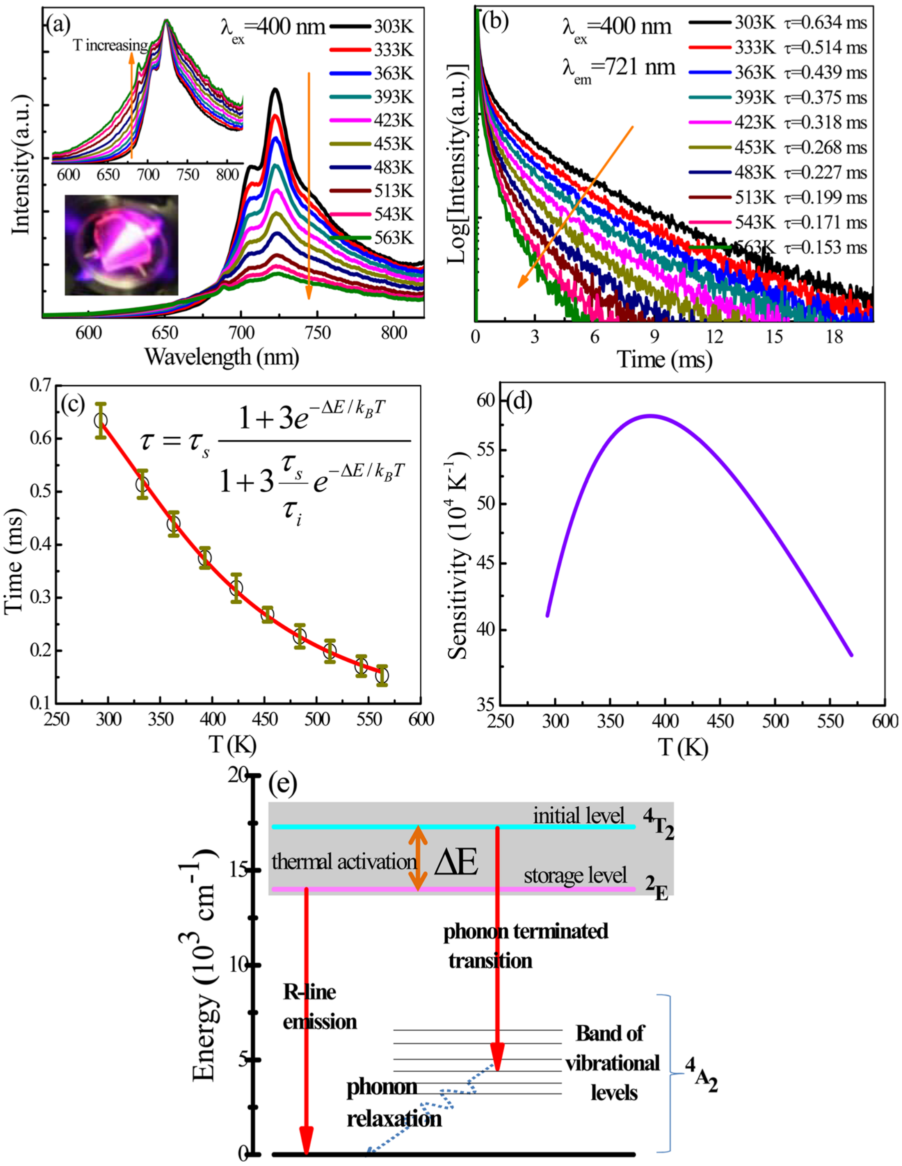

Figure 8. (a) Impact of temperature (303−563 K) on Cr^{3+} PL spectra in the $Yb^{3+}/Er^{3+}/Cr^{3+}$ triply doped GC-A sample. Insets are normalized emission spectra (top) and luminescent photograph (bottom). (b) Cr^{3+} decay curves versus temperature. (c) Temperature-dependent experimental lifetimes of Cr^{3+} in GC-A sample and the fitting curve. (d) Dependence of sensing sensitivity on temperature. (e) Two-level model for Cr^{3+} luminescence in the dual-phase glass ceramic.

for FIR-based temperature sensing due to the competition of UC luminescence from the thermal coupling Er^{3+} $^2H_{11/2}$ and $^4S_{3/2}$ excited states, as schematically illustrated in the Figure 5. Importantly, such spatial isolation strategy for the different active ions in the dual-phase glass ceramic will effectively lessen adverse energy transfer (ET) between RE^{3+} and Cr^{3+} (Figure 5), leading to intense Er^{3+} anti-Stokes and Cr^{3+} Stokes emissions simultaneously. UC emission spectra and decay curves of the $Yb^{3+}/Er^{3+}/Cr^{3+}$ (1/0.1/x mol %) triply doped PG and GC-A samples with various Cr^{3+} contents (donated PG0, PG0.2, PG1 and GC0, GC0.2, GC1 for x = 0, 0.2, and 1, respectively) were recorded under 980 nm NIR laser excitation. Obviously, the Er^{3+} UC luminescence greatly weakens with increase of Cr^{3+} content in the PG samples, as shown in Figure 6a, confirming the existence of adverse ETs from Er^{3+} to Cr^{3+} ions in the PG samples. Evidently, the decay lifetime of the $^2H_{11/2}$,$^4S_{3/2}$ states of Er^{3+} in PG decreases from 0.090 to 0.076 ms with increase of Cr^{3+} content from 0 to 1 mol % (Figure 6b) due to the adverse energy transfer from Er^{3+}: $^2H_{11/2}$,$^4S_{3/2}$ states to Cr^{3+}: $^4T_2$(F). On the other hand, the corresponding lifetime of Er^{3+} in the dual-phase glass ceramic is almost unchanged with increase of Cr^{3+} content, as demonstrated in Figure 6c,d. These results confirm that the “dopant isolation” strategy is an efficient way to reduce the adverse energy transfers between Er^{3+} and Cr^{3+} in the present dual-phase glass ceramic.

Finally, to explore the possible applications of the present dual-phase GC in optical temperature sensors, temperature-dependent UC emission spectra of the $Yb^{3+}/Er^{3+}/Cr^{3+}$ triply doped GC-A sample were recorded in the temperature ranging from 303 to 563 K under 980 nm NIR laser excitation. As depicted in Figure 7a, it can be clearly observed that these spectra exhibit two distinct emission bands around 520 and 539 nm assigned to the $^2H_{11/2} \rightarrow {}^4I_{15/2}$ and $^4S_{3/2} \rightarrow {}^4I_{15/2}$ transitions of Er^{3+} ions, respectively. The integrated FIR of these two UC emission bands shows an obvious dependence on the temperature (Figure 7b) due to the thermal couple between $^2H_{11/2}$ and $^4S_{3/2}$ states of Er^{3+}

Table 3. Optical Thermometry Parameters for Some Typical Er^{3+} Doped UC Materials and Cr^{3+} Doped Crystals

optical thermometric medium	ΔE (cm^{-1})	C	T_{max} (K)	max sensitivity (% K^{-1})	ref
			Er^{3+}		
silicate glass	895	7.92	550	0.31	22
fluoroindate glass	770	11.2	550	0.55	42
β-$NaYF_4$ NCs	752	8.06	535	0.40	21
α-$NaYF_4$ GC	775	4.89	560	0.24	3
β-$NaYF_4$ GC	789	7.71	580	0.37	35
YF_3 + Ga_2O_3 GC	717	4.66	514	0.25	this work
			Cr^{3+}		
$MgAl_2O_4$				0.37	43
$YAlO_3$				0.19	43
$Y_3Al_5O_{12}$				0.50	44
$LiAl_5O_8$			447	0.83	5
ruby (Al_2O_3)	1637		390	0.48	45
YF_3 + Ga_2O_3 GC	1215		386	0.59	this work

ions. FIR of these two thermally coupled levels can be easily deduced on the basis of the Boltzmann distribution theory:[2]

$$\mathrm{FIR} = \frac{I_{520}}{I_{539}} = \frac{g_H A_H \sigma_H w_H}{g_S A_S \sigma_S w_S} \exp\left(\frac{-\Delta E}{k_B T}\right) = C \exp\left(\frac{-\Delta E}{k_B T}\right) \quad (4)$$

Here, C is the constant; I_{520} and I_{539} are the integrated UC intensities corresponding to the ${}^2H_{11/2} \rightarrow {}^4I_{15/2}$ and ${}^4S_{3/2} \rightarrow {}^4I_{15/2}$ transitions of Er^{3+}, respectively; T is the absolute temperature; ΔE is the energy gap between ${}^2H_{11/2}$ and ${}^4S_{3/2}$ states; k_B is the Boltzmann constant; and g, A, σ, and w are the degeneracy, the spontaneous radiative transition rate, the emission cross-section, and the angular frequency of fluorescent transitions from the ${}^2H_{11/2}$ or ${}^4S_{3/2}$ excited state to the ${}^4I_{15/2}$ ground state of Er^{3+}, respectively.

On the basis of eq 4, $\ln(I_{520}/I_{539})$ is plotted against inverse absolute temperature, as presented in Figure 7c. The slope and intercept can be obtained and are equal to 1031 ± 33 and 1.54 ± 0.08, respectively, via the linear fitting of experiment data. As a result, the energy gap ΔE and constant C are evaluated to be about 717 cm^{-1} and 4.66, respectively, which are important factors for the sensor sensitivity (S) of temperature detecting, as given by the following equation:[2,41]

$$S = \frac{\mathrm{d(FIR)}}{\mathrm{d}T} = \mathrm{FIR}\left(\frac{\Delta E}{k_B T^2}\right) = C\left(\frac{\Delta E}{k_B T^2}\right)\exp\left(\frac{-\Delta E}{k_B T}\right) \quad (5)$$

The calculated curve of sensing sensitivity as a function of absolute temperature is plotted in Figure 7d. It is found that the sensitivity gradually increases with increase of temperature from 303 to 514 K, where the maximal sensitivity of about 0.25% K^{-1} is achieved, and then decreases when further increasing temperature.

Furthermore, the PL and decay behaviors of Cr^{3+} in the $Yb^{3+}/Er^{3+}/Cr^{3+}$ triply doped GC-A sample were also investigated under 400 nm blue light excitation in the temperature ranging from 303 to 563 K. Evidently, both the emission intensities of the sharp line that originated from the Cr^{3+} ${}^2E \rightarrow {}^4A_2$ transition and broadband background assigned to the ${}^4T_2 \rightarrow {}^4A_2$ transition are highly affected by the recording temperature, as exhibited in Figure 8a. Increasing temperature induces a slight increase of the broadband emission with a gradual decrease of the sharp one. As shown in the inset of Figure 8a, the normalized emission spectra show this relative intensity variation, which is believed to be attributed to the thermal coupling between ${}^2E$ and ${}^4T_2$ states of Cr^{3+} in the γ-Ga_2O_3 phase. At high temperature, the Cr^{3+} ${}^4T_2 \rightarrow {}^4A_2$ transition luminescence is dominated in the emission spectrum. More importantly, temperature is revealed to have an important influence on the Cr^{3+} fluorescence lifetime, as shown in Figure 8b. The Cr^{3+} lifetime value monotonously decreases from 0.634 to 0.153 ms (Figure 8c), as the temperature is elevated from 303 to 563 K. In the present dual-phase GC, the ${}^2E$ state of Cr^{3+} is the lowest excited state at room temperature because of the incorporation of Cr^{3+} dopants in the γ-Ga_2O_3 crystallized phase with high crystal-field strength ($Dq/B = 2.46 > 2.30$). At low temperature, the luminescence primarily originates from the spin-forbidden ${}^2E$ state (${}^2E \rightarrow {}^4T_2$) so that a long lifetime is expected. At the high temperature, thermal activation will result in an increase in the population of the short lifetime ${}^4A_2$ state, thus leading to a decrease in the Cr^{3+} fluorescence lifetime.

Herein, a two-level kinetic model, including an "initial state" (${}^4T_2$) and a "storage one" (${}^2E$), is adopted to fit the lifetime variation with increase of temperature,[20] as schematically exhibited in Figure 8e. Notably, this model assumed that the transitions of the excited Cr^{3+} ions to the ground state all originated from the above-mentioned two excited states. In fact, such a model has been successfully used to describe vibronic laser action in alexandrite (Cr^{3+}: $BeAl_2O_4$) previously.[20] On the basis of this model, the modification of the total amount of electrons (n) in the ${}^4T_2$ and ${}^2E$ levels is expressed by the rate equation

$$\frac{\mathrm{d}n}{\mathrm{d}t} = -\frac{1}{\tau_s} n_s - \frac{1}{\tau_i} n_i \quad (6)$$

where τ_s and τ_i are the fluorescence lifetimes of ${}^2E$ and ${}^4T_2$ states, respectively, $n = n_i + n_s$, and n_i and n_s are the populations of ${}^4T_2$ and ${}^2E$ levels. Moreover, these two thermal coupling levels should follow the Boltzmann distribution because of the "quasi-thermodynamic equilibrium" between ${}^2E$ and ${}^4T_2$ levels

$$\frac{n_i}{n_s} = Ce^{-\Delta E/k_B T} \quad (7)$$

where ΔE is the energy gap between ${}^4T_2$ and ${}^2E$ states, T is the absolute temperature, C is the ratio of the degeneracy of ${}^4T_2$ to that of ${}^2E$, with a value of 3, and k_B is Boltzmann constant. Consequently, according to eqs 6 and 7, the temperature-dependent lifetime can be deduced as[15,20]

$$\tau = \tau_s \frac{1 + Ce^{-\Delta E/k_BT}}{1 + C\frac{\tau_s}{\tau_i}e^{-\Delta E/k_BT}} = \tau_s \frac{1 + 3e^{-\Delta E/k_BT}}{1 + 3\frac{\tau_s}{\tau_i}e^{-\Delta E/k_BT}} \tag{8}$$

where τ is the fluorescence lifetime of Cr^{3+} in GC. Accordingly, the solid line drawn in Figure 8c is the least-squares fitting of eq 8 to the lifetime data ranging from 303 to 563 K for the $Yb^{3+}/Er^{3+}/Cr^{3+}$ triply doped dual-phase GC sample. Importantly, the correlation coefficient (r^2) reaches as high as 0.999, confirming that eq 8 fits the temperature-dependent lifetime quite well in the experimental temperature range. As a result, the corresponding ΔE, τ_s, and τ_i parameters in eq 8 are determined to be 1215 cm^{-1}, 0.790 ms, and 22.6 μs, respectively. Subsequently, the sensor sensitivity (S) of temperature detection is obtained with the help of these parameters, as expressed by the following equation:

$$\begin{aligned} S &= \left|\frac{1}{\tau}\frac{d\tau}{dT}\right| \\ &= 3e^{-\Delta E/k_BT} \times \frac{\Delta E}{k_BT^2} \times \left(\frac{1}{1 + 3e^{-\Delta E/k_BT}} \right. \\ &\quad \left. - \frac{\tau_s}{\tau_i + 3\tau_s e^{-\Delta E/k_BT}}\right) \end{aligned} \tag{9}$$

Figure 8d shows the temperature-dependent sensor sensitivity curve. Obviously, the sensitivity monotonously increases and reaches the maximal value of 0.59% K^{-1} at 386 K, and then gradually decreases with further increasing temperature.

As a comparison, several important thermometry parameters for some related Yb^{3+}/Er^{3+} codoped UC materials and Cr^{3+} doped crystals are listed in Table 3. Unlike Yb^{3+}/Er^{3+} codoped silicate glass, greatly enhanced UC optical performance is realized in the investigated dual-phase glass ceramic because of the low-phonon-energy YF_3 crystalline environment of the lanthanide activators (Yb^{3+}/Er^{3+}). Moreover, the GC embedding with YF_3 NCs shows better stability than pure fluoride (such as $NaYF_4$) powders ascribing to efficient protection of YF_3 NCs by the aluminosilicate glass matrix. On the other hand, as an alternative for single-crystal materials, the investigated GC containing dual-phase NCs not only takes advantages of easy fabrication with the help of the cost-efficient and fast glass-melting route, but also exhibits excellent temperature sensing characteristic owing to the suitable crystal-field environment of Cr^{3+} dopants. Importantly, after several cycle experiments, the repeatability of temperature sensing based on the FIR of Er^{3+} ions and fluorescence lifetime of Cr^{3+} ions in the present dual-phase GC is quite good. Therefore, we believe that such transparent $Yb^{3+}/Er^{3+}/Cr^{3+}$ triply doped β-YF_3 and γ-Ga_2O_3 dual-phase NCs embedded glass ceramic sample with efficient anti-Stokes and Stokes luminescent feature is a very promising candidate for the application in the dual-modal fiber temperature sensors.

■ CONCLUSION

In summary, $Yb^{3+}/Er^{3+}/Cr^{3+}$ triply doped oxyfluoride glasses were successfully synthesized by a traditional melt-quenching technique. After glass crystallization treatment, cubic γ-Ga_2O_3 nanoparticles and orthorhombic β-YF_3 nanocrystals embedded bulk glass ceramics were realized where Cr^{3+} dopants were evidenced to partition into the Ga_2O_3 nanocrystals while Yb^{3+}/Er^{3+} ones entered into the YF_3 crystalline lattice. As a result, the adverse energy transfers between Er^{3+} and Cr^{3+} were greatly suppressed owing to the spatial separation of these two different active ions, being beneficial to the achievement of both intense deep-red luminescence corresponding to Cr^{3+}: $^2E \rightarrow {}^4A_2$ transition and green upconversion emissions ascribing to Er^{3+}: $^2H_{11/2},{}^4S_{3/2} \rightarrow {}^4I_{15/2}$ transitions. Importantly, strong temperature-dependent decay of Cr^{3+} was observed since a high percentage of the excited Cr^{3+} ions in the long lifetime ^2E state will be populated to the short lifetime $^4T_2$ state via thermal activation with increase of temperature; in the meantime, obvious temperature-dependent upconversion fluorescence intensity ratio between Er^{3+}: $^2H_{11/2} \rightarrow {}^4I_{15/2}$ transition and $^4S_{3/2} \rightarrow {}^4I_{15/2}$ one was detected owing to the competitive radiation transitions from these two thermally coupled emitting states. Using the fabricated glass ceramic as the optical thermometric medium, the temperature sensitivities can reach as high as 0.25% K^{-1} at 514 K based on Er^{3+} upconversion luminescence and 0.59% K^{-1} at 386 K based on Cr^{3+} fluorescence decay, respectively. We believe that the present $Yb^{3+}/Er^{3+}/Cr^{3+}$ dual-phase glass ceramic with efficient dual-modal temperature-dependent luminescence might be a very promising candidate for accurate optical temperature sensing.

■ AUTHOR INFORMATION

Corresponding Author

*E-mail: dqchen@hdu.edu.cn.

Notes

The authors declare no competing financial interest.

■ ACKNOWLEDGMENTS

This work was supported by the Graduate Scientific Research Foundation of Hangzhou Dianzi University (KYJJ2014018), the 151 talent's projects in the second level of Zhejiang Province, the Natural Science Foundation of Zhejiang Province for Distinguished Young Scholars (LR15E020001), the Natural Science Foundation of Fujian Province (2015J01632), and National Natural Science Foundation of China (21271170, 61372025, 51572065).

■ REFERENCES

(1) Brübach, J.; Pflitsch, C.; Dreizler, A.; Atakan, B. On Surface Temperature Measurements with Thermographic Phosphors: a Review. *Prog. Energy Combust. Sci.* **2013**, *39*, 37−60.

(2) Dong, B.; Cao, B. S.; He, Y. Y.; Liu, Z.; Li, Z. P.; Feng, Z. Q. Temperature Sensing and In Vivo Imaging by Molybdenum Sensitized Visible Upconversion Luminescence of Rare-Earth Oxides. *Adv. Mater.* **2012**, *24*, 1987−1993.

(3) Dey, R.; Rai, V. K. Yb^{3+} Sensitized Er^{3+} Doped La_2O_3 Phosphor in Temperature Sensors and Display Devices. *Dalton Trans.* **2014**, *43*, 111−118.

(4) Jiang, S.; Zeng, P.; Liao, L. Q.; Tian, S. F.; Guo, H.; Chen, Y. H.; Duan, C. K.; Yin, M. Optical Thermometry Based on Upconverted Luminescence in Transparent Glass Ceramics Containing $NaYF_4$:Yb^{3+}/Er^{3+} Nanocrystals. *J. Alloys Compd.* **2014**, *617*, 538−541.

(5) Li, X. Y.; Jiang, G. C.; Zhou, S. S.; Wei, X. T.; Chen, Y. H.; Duan, C. K. Luminescent Properties of Chromium(III)-doped Lithium Aluminate for Temperature Sensing. *Sens. Actuators, B* **2014**, *202*, 1065−1069.

(6) Huang, F.; Gao, Y.; Zhou, J. C.; Xu, J.; Wang, Y. S. Yb^{3+}/Er^{3+} Co-doped $CaMoO_4$: A Promising Green Upconversion Phosphor for Optical Temperature Sensing. *J. Alloys Compd.* **2015**, *639*, 325−329.

(7) Zheng, W. C.; Li, B. X.; Feng, G. Y.; Liu, H. G. Research on the Thermal Shifts and Electron−phonon Coupling Parameters of R-line for Cr^{3+} and Mn^{4+} ions in $YAlO_3$ Crystals. *J. Lumin.* **2013**, *138*, 214−217.

(8) Pandey, A.; Rai, V. K.; Kumar, V.; Kumar, V.; Swart, H. C. Upconversion Based Temperature Sensing Ability of Er^{3+}-Yb^{3+} Codoped $SrWO_4$: An Optical Heating Phosphor. *Sens. Actuators, B* **2015**, *209*, 352−358.

(9) Mahata, M. K.; Kumar, K.; Rai, V. K. Er^{3+}-Yb^{3+} Doped Vanadate Nanocrystals: A Highly Sensitive Thermographic Phosphor and its Optical Nanoheater Behavior. *Sens. Actuators, B* **2015**, *209*, 775−780.

(10) Xu, W.; Zhao, H.; Zhang, Z. G.; Cao, W. W. Highly Sensitive Optical Thermometry through Thermally Enhanced near Infrared Emissions from Nd^{3+}/Yb^{3+} Codoped Oxyfluoride Glass Ceramic. *Sens. Actuators, B* **2013**, *178*, 520−524.

(11) Ye, L.; Zhang, J.; Shi, Y. Growth and Characteristics of Cr^{3+}:YAG Crystal Fiber for Fluorescence Decay Temperature Sensor. *Rev. Sci. Instrum.* **2006**, *77*, 054901.

(12) Wade, S. A.; Collins, S. F.; Baxter, G. W. Fluorescence Intensity Ratio Technique for Optical Fiber Point Temperature Sensing. *J. Appl. Phys.* **2003**, *94*, 4743−4756.

(13) Reddy, B. R.; Kamma, I.; Kommidi, P. Optical Sensing Techniques for Temperature Measurement. *Appl. Opt.* **2013**, *52*, B33−B39.

(14) Khalid, A. H.; Kontis, K. Thermographic Phosphors for High Temperature Measurements: Principles, Current State of the Art and Recent Applications. *Sensors* **2008**, *8*, 5673−5744.

(15) Zhang, Z. Y.; Grattan, K. T. V.; Palmer, A. W. Temperature Dependences of Fluorescence Lifetimes in Cr^{3+}-doped Insulating Crystals. *Phys. Rev. B: Condens. Matter Mater. Phys.* **1993**, *48*, 7772−7778.

(16) Hu, Y. L.; Zhang, Z. Y.; Grattan, K. T. V.; Palmer, A. W.; Meggitt, B. T. Ruby-based Decay-time Thermometry: Effect of Probe Size on Extended Measurement Range (77−800K). *Sens. Actuators, A* **1997**, *63*, 85−90.

(17) Uchiyama, H.; Aizawa, H.; Katsumata, T.; Komuro, S.; Morikawa, T.; Toba, E. Fiber-optic Thermometer Using Cr-doped $YAlO_3$ Sensor Head. *Rev. Sci. Instrum.* **2003**, *74*, 3883−3885.

(18) Shen, Y. R.; Bray, K. L. Effect of Pressure and Temperature on the Lifetime of Cr^{3+} in Yttrium Aluminum Garnet. *Phys. Rev. B: Condens. Matter Mater. Phys.* **1997**, *56*, 10882−10891.

(19) Kitaoka, Y.; Nakamura, K.; Akiyama, T.; Ito, T.; Weinert, M.; Freeman, A. J. Excited Cr Impurity States in Al_2O_3 from Constraint Density Functional Theory. *Phys. Rev. B: Condens. Matter Mater. Phys.* **2013**, *87*, 205113.

(20) Walling, J. C.; Peterson, O. G.; Jenssen, H. P.; Morris, R. C.; O'Dell, E. W. Tunable Alexandrite Lasers. *IEEE J. Quantum Electron.* **1980**, *16*, 1302−1315.

(21) Zhou, S. H.; Deng, K. M.; Wei, X. T.; Jiang, G. C.; Duan, C. K.; Chen, Y. H.; Yin, M. Upconversion Luminescence of $NaYF_4$: Yb^{3+}, Er^{3+} for Temperature Sensing. *Opt. Commun.* **2013**, *291*, 138−142.

(22) Zhou, S. Q.; Li, C. G.; Liu, Z. F.; Li, S. F.; Song, C. L. Thermal Effect on Up-conversion in Er^{3+}/Yb^{3+} Co-doped Silicate Glass. *Opt. Mater.* **2007**, *30*, 513−516.

(23) Chen, D. Q.; Chen, Y.; Lu, H. W.; Ji, Z. G. A Bifunctional Cr/Yb/Tm: $Ca_3Ga_2Ge_3O_{12}$ Phosphor with Near-Infrared Long-Lasting Phosphorescence and Upconversion Luminescence. *Inorg. Chem.* **2014**, *53*, 8638−8645.

(24) Zhou, S. F.; Jiang, N.; Miura, K.; Tanabe, S.; Shimizu, M.; Sakakura, M.; Shimotsuma, Y.; Nishi, M.; Qiu, J. R.; Hirao, K. Simultaneous Tailoring of Phase Evolution and Dopant Distribution in the Glassy Phase for Controllable Luminescence. *J. Am. Chem. Soc.* **2010**, *132*, 17945−17952.

(25) Lin, H.; Zhang, R.; Chen, D. Q.; Yu, Y. L.; Yang, A. P.; Wang, Y. S. Tuning of Multicolor emissions in Glass Ceramics Containing γ-Ga_2O_3 and β-YF_3 Nanocrystals. *J. Mater. Chem. C* **2013**, *1*, 1804−1811.

(26) Page, R. H.; Schaffers, K. I.; Waide, P. A.; Tassano, J. B. Upconversion-pumped Luminescence Efficiency of Rare-earth-doped Hosts Sensitized with Trivalent Ytterbium. *J. Opt. Soc. Am. B* **1998**, *15*, 996.

(27) Gao, G. J.; Peng, M. Y.; Wondraczek, L. Temperature Dependence and Quantum Efficiency of Ultrabroad NIR Photoluminescence from Ni^{2+} Centers in Nanocrystalline Ba-Al Titanate Glass Ceramics. *Opt. Lett.* **2012**, *37*, 1166−1168.

(28) Zhuang, Y. X.; Ueda, J.; Tanabe, S. Multi-color Persistent Luminescence in Transparent Glass Ceramics Containing Spinel Nanocrystals with Mn^{2+} Ions. *Appl. Phys. Lett.* **2014**, *105*, 191904.

(29) Chenu, S.; Veron, E.; Genevois, C.; Matzen, G.; Cardinal, T.; Etienne, A.; Massiot, D.; Allix, M. Tunuineable Nanostructuring of Highly Transparent Zinc Gallogermanate Glasses and Glass-Ceramics. *Adv. Opt. Mater.* **2014**, *2*, 364−372.

(30) Zhang, X. J.; Huang, L.; Pan, F. J.; Wu, M. M.; Wang, J.; Chen, Y.; Su, Q. Highly Thermally Stable Single-Component White-Emitting Silicate Glass for Organic-Resin-Free White-Light-Emitting Diodes. *ACS Appl. Mater. Interfaces* **2014**, *6*, 2709−2717.

(31) Skrzypczak, U.; Seifert, G.; Schweizer, S. Highly Efficient and Broadband Upconversion of NIR Sunlight with Neodymium-Doped Glass Ceramics. *Adv. Opt. Mater.* **2015**, *3*, 541−545.

(32) Zhou, S. F.; Li, C. Y.; Yang, G.; Bi, G.; Xu, B. B.; Hong, Z. L.; Miura, K.; Hirao, K.; Qiu, J. R. Self-Limited Nanocrystallization-mediated Activation of Semiconductor Nanocrystal in an Amorphous Solid. *Adv. Funct. Mater.* **2013**, *23*, 5436−5443.

(33) Fedorov, P. P.; Luginina, A. A.; Popov, A. I. Transparent Oxyfluoride Glass Ceramics. *J. Fluorine Chem.* **2015**, *172*, 22−50.

(34) Lin, H.; Wang, B.; Xu, J.; Zhang, R.; Chen, H.; Yu, Y. L.; Wang, Y. S. Phosphor-in-Glass for High-Powered Remote-Type White AC-LED. *ACS Appl. Mater. Interfaces* **2014**, *6*, 21264−21269.

(35) Chenu, S.; Veron, E.; Genevois, C.; Garcia, A.; Matzen, G.; Allix, M. Long-Lasting Luminescent $ZnGa_2O_4$:Cr^{3+} Transparent Glass-Ceramics. *J. Mater. Chem. C* **2014**, *2*, 10002−10010.

(36) Cheng, Q.; Sui, J.; Cai, W. Enhanced Upconverison Emission in Yb^{3+} and Er^{3+} codoped $NaGdF_4$ Nanocrystals by Introducing Li^{+} Ions. *Nanoscale* **2012**, *4*, 779−784.

(37) Viana, B.; Lejus, A. M.; Vivien, D.; Poncon, V.; Boulon, G. Synthesis, ESR Investigation, and Optical Properties of the Potential Vibronic Laser Material $LaMgAl_{11}$-xCr_xO_{19}. *J. Solid State Chem.* **1987**, *71*, 77−86.

(38) Xu, J.; Chen, D. Q.; Yu, Y. L.; Zhu, W. J.; Zhou, J. C.; Wang, Y. S. Cr^{3+}:$SrGa_{12}O_{19}$: A Broadband Near-Infrared Long-Persistent Phosphor. *Chem. - Asian J.* **2014**, *9*, 1020−1025.

(39) O'Donnell, K. P.; Marshall, A.; Yamaga, M.; Henderson, B.; Cockayne, B. Vibronic Structure in the Photoluminescence Spectrum of Cr^{3+} Ions in Garnets. *J. Lumin.* **1989**, *42*, 365−373.

(40) Casalboni, M.; Luci, A.; Grassano, U. M.; Mill, B. V.; Kaminskii, A. A. Optical Spectroscopy of $La_3Ga_5SiO_{14}$:Cr^{3+} Crystals. *Phys. Rev. B: Condens. Matter Mater. Phys.* **1994**, *49*, 3781.

(41) Zheng, K. Z.; Liu, Z. Y.; Lv, C. J.; Qin, W. P. Temperature Sensor Based on the UV Upconversion Luminescence of Gd^{3+} in Yb^{3+}-Tm^{3+}-Gd^{3+} Codoped $NaLuF_4$ Microcrystals. *J. Mater. Chem. C* **2013**, *1*, 5502−5507.

(42) Maciel, G. S.; Menezes, L. de S.; Gomes, A. S. L.; de Araújo, C. B.; Messaddeq, Y.; Florez, A.; Aegerter, M. A. Temperature Sensor Based on Frequency Upconversion in Er^{3+}-doped Fluoroindate Glass. *IEEE Photonics Technol. Lett.* **1995**, *7*, 1474−1476.

(43) Uchiyama, H.; Aizawa, H.; Katsumata, T.; Komuro, S.; Morikawa, T.; Toba, E. Fiber-optic Thermometer Using Cr-doped $YAlO_3$ Sensor Head. *Rev. Sci. Instrum.* **2003**, *74*, 3883−3885.

(44) Aizawa, H.; Katsumata, T.; Kiyokawa, Y.; Nishikawa, T.; Sasagawa, T.; Komuro, S.; Morikawa, T.; Ishizawa, H.; Toba, E. Evaluation of Cr-doped Yttrium Aluminum Garnet Crystals for Hybrid Fiber-optic Thermometer Application. *Measurement* **2006**, *39*, 147−152.

(45) Seat, H. C.; Sharp, J. H. Dedicated Temperature Sensing With C-Axis Oriented Single-Crystal Ruby (Cr^{3+}: Al_2O_3) Fibers: Temperature and Strain Dependences of R-Line Fluorescence. *IEEE Trans. Instrum. Meas.* **2004**, *53*, 140−154.